J. Fluid Mech. (2025), *vol.* 1020, A39, doi:10.1017/jfm.2025.10664

On the oscillatory dynamics of a Saffman–Taylor finger with a bubble at its tip

Jack Lawless[1,3], **Andrew L. Hazel**[2,3] **and Anne Juel**[1,3]

[1]Physics of Fluids & Soft Matter, Department of Physics & Astronomy, University of Manchester, Manchester M13 9PL, UK

[2]Department of Mathematics, University of Manchester, Manchester M13 9PL, UK

[3]Manchester Centre for Nonlinear Dynamics, University of Manchester, Oxford Road, Manchester M13 9PL, UK

Corresponding author: Anne Juel, anne.juel@manchester.ac.uk

(Received 31 May 2025; revised 16 August 2025; accepted 4 September 2025)

The complex behaviour of air–liquid interfaces driven into Hele-Shaw channels at high speeds could arise from oscillatory dynamics; yet both the physical and dynamical mechanisms that lead to interfacial oscillations remain unclear. We extend the experiments by Couder *et al.* (1986, *Phys. Rev. A,* vol. 34, 5175) to present a systematic investigation of the dynamics that results when a small air bubble is placed at the tip of a steadily propagating air finger in a horizontal Hele-Shaw channel. The system can exhibit steady and oscillatory behaviours, and we show that these different behaviours each occur in well-defined regions of the phase space defined by flow rate and bubble size. For sufficiently large flow rates, periodic finger oscillations give way to disordered dynamics characterised by an irregular meandering of the finger's tip. At fixed flow rate, the oscillations commence when the bubble size is increased sufficiently that the decreased curvature of the bubble tip in the horizontal plane matches that of the finger tip. This causes the axial pressure gradient along the bubble to vanish, thus rendering the bubble susceptible to lateral perturbations. Differing time scales for finger and bubble restoral allow sustained oscillations to develop in the finger–bubble system. The oscillations cease when the bubble is sufficiently large that it can act as the tip of a single finger. The disordered dynamics at high flow rates are consistent with the transient exploration of unstable periodic states, which suggests that similar dynamics may underlie disorder in viscous fingering.

Key words: fingering instability, Hele-Shaw flows, nonlinear instability

© The Author(s), 2025. Published by Cambridge University Press. This is an Open Access article, distributed under the terms of the Creative Commons Attribution licence (https://creativecommons.org/licenses/by/4.0/), which permits unrestricted re-use, distribution and reproduction, provided the original article is properly cited.

https://doi.org/10.1017/jfm.2025.10664 Published online by Cambridge University Press

1. Introduction

The displacement of a more-viscous fluid by a less-viscous fluid inside a quasi-two-dimensional (Hele-Shaw) channel gives rise to a fascinating pattern-forming phenomenon known as viscous fingering (Couder 2003); see figure 1. At low propagation speeds, the interface between the two fluids takes the shape of a single symmetric finger (figure 1*a*), known as a Saffman–Taylor finger (Saffman & Taylor 1958). At higher speeds, but still driven by a constant flow rate, complex interfacial patterns can develop (figure 1*b*). The patterns are formed by the growth of intricate finger-like protrusions at the morphologically unstable interface between the two fluids, and the detailed dynamics depends on the channel's geometry, fluid miscibility, and propagation speed of the interface (Dias *et al.* 2012; Bischofberger, Ramachandran & Nagel 2014; Zheng, Kim & Stone 2015; Juel, Pihler-Puzović & Heil 2018). The allure of these patterns stems from their irregularity, which is a direct consequence of the system's propensity to exhibit 'disordered' growth dynamics (Paterson 1981; Chen 1989; Arnéodo *et al.* 1989; Kopf-Sill & Homsy 1988). Whilst attempts have been made to characterise these patterns from a phenomenological perspective, with morphological descriptions such as their fractal dimensions (Zhang & Liu 1998; Mathiesen *et al.* 2006; Beeson-Jones & Woods 2019) being used to quantify their complexity, the underlying drivers of the system's disordered dynamics have remained poorly understood from both a dynamical systems and physical perspective (Lawless, Juel & Pihler-Puzović 2025). We are particularly interested in periodic dynamics because unstable periodic states can be the 'building blocks' of disordered dynamics, as highlighted in studies of the subcritical transition to turbulence in linearly stable wall-bounded shear flows, where analysis of unstable periodic states has led to significant progress in understanding the time-averaged statistical properties of turbulent flows (Duguet, Pringle & Kerswell 2008; Eckhardt *et al.* 2008; Kawahara, Uhlmann & van Veen 2012; Budanur *et al.* 2017; Cvitanović & Gibson 2010; Suri *et al.* 2020). We hypothesise that the complex time-dependent behaviour of viscous fingers is orchestrated by (dynamically disconnected) unstable periodic states, which motivates the present experimental investigation into periodic propagation dynamics.

Previous experiments have shown that Saffman–Taylor fingers become increasingly sensitive to perturbations as the driving parameter is increased (Tabeling, Zocchi & Libchaber 1987; Chevalier, Lindner & Clément 2007), and the nonlinear stability analysis performed by Bensimon (1986) indicates that the amplitude of perturbation required for instability decreases exponentially with increasing values of this driving parameter. Perturbations of the finger tip can lead to selection of 'anomalous' steadily propagating fingers: introduction of a thin thread (Zocchi *et al.* 1987) leads to narrower symmetric or asymmetric fingers; the presence of a bubble at the finger tip (Couder, Gérard & Rabaud 1986) can also lead to narrower fingers, a finding later confirmed theoretically (Hong & Langer 1987; Combescot & Dombre 1989); etching grooves or a microscopic lattice into a channel boundary (Rabaud, Couder & Gerard 1988; McCloud & Maher 1995) also leads to similar long-term behaviours.

In this paper, we revisit the experiments originally carried out by Couder *et al.* (1986), in which the Saffman–Taylor finger was perturbed by placing a bubble at its tip. The bubble provides a unique means of perturbing the tip of the finger because, unlike channel geometry perturbations, this perturbation remains localised to the tip of the finger as it propagates. The original experiments were motivated by the so-called finger selection problem, which concerns the associated depth-averaged lubrication theory's lack of a selection mechanism in the absence of surface tension for the half-width finger observed in experiments (Saffman & Taylor 1958). However, Couder *et al.* (1986) also uncovered the

https://doi.org/10.1017/jfm.2025.10664 Published online by Cambridge University Press

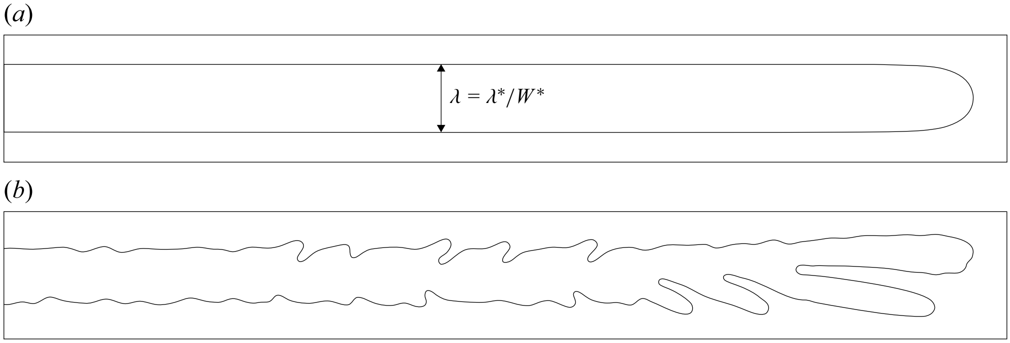

Figure 1. The typical fingering patterns that develop when a constant flux of air invades a viscous liquid-filled Hele-Shaw channel at two different values of the dimensionless parameter $1/B = 12\alpha^2\, Ca$, where $\alpha = W^*/H^*$ is the channel's cross-sectional aspect ratio, and $Ca = \mu U^*/\sigma$ is a capillary number. Here, μ is the dynamic viscosity of the liquid, σ is the surface tension at the air–liquid interface, and U^* is the finger's propagation speed. (*a*) The single, steadily propagating and symmetric Saffman–Taylor finger that develops for $1/B = 1200$. The channel's width is $W^* = 40.0 \pm 0.1$ mm, and its depth is $H^* = 1.00 \pm 0.01$ mm. The liquid's dynamic viscosity is $\mu = 0.019$ Pa s. The finger width λ^* is also indicated. (*b*) The disordered finger that develops for $1/B = 15\,000$. The channel's width is $W^* = 60.0 \pm 0.1$ mm, and its depth is $H^* = 1.00 \pm 0.01$ mm. The liquid's dynamic viscosity is $\mu = 0.095$ Pa s. The surface tension at the air–liquid interface is $\sigma = 21$ mN m^{-1} in both cases. This figure has been reproduced from Lawless, Hazel & Juel (2024) with permission.

propagation of dynamically intriguing fingers with either laterally oscillating or pulsating tips.

The preliminary observations of periodic oscillations by Couder *et al.* (1986) have since been complemented by similar findings in other geometrically perturbed systems. For example, the depth-perturbed system studied by Hazel *et al.* (2013) contains a multitude of stable and unstable periodic states (Pailha *et al.* 2012; Keeler *et al.* 2019; Lawless *et al.* 2022). The experiments by Cuttle, Pihler-Puzović & Juel (2020) inside elasto-rigid Hele-Shaw channels, where the channel's upper boundary was replaced by a deformable elastic membrane, also revealed complex unsteady dynamics; and a host of periodic states were found by Fontana *et al.* (2024) in a model of that system. The most comprehensive study of periodic dynamics was carried out by Lawless *et al.* (2024), who initiated stable oscillations by remotely perturbing the finger's tip with neighbouring bubbles. These studies clearly demonstrate that the finger has a propensity to exhibit oscillations when controlled perturbations are applied, but these perturbations typically modify the system's bifurcation structure, and it is indeed possible that the oscillatory states do not exist in the unperturbed system, although there is theoretical evidence for a countably infinite number of unstable steadily propagating states (Romero 1982; Vanden-Broeck 1983; Gardiner, McCue & Moroney 2015).

The principal aim of the present paper is to examine the mechanisms that lead to the observed periodic oscillations by systematically varying the bubble's size and flow rate in experiments in order to establish empirical criteria for when the steadily propagating finger destabilises. For sufficiently large flow rates, our experiments also reveal novel disordered finger dynamics, which are consistent with the transient exploration of multiple unstable periodic states.

We have organised the paper as follows. First, the experimental set-up and methods used to generate and propagate bubbles are described in § 2.1. Because the underlying physical mechanism that leads to periodic dynamics requires prior knowledge of the single Saffman–Taylor finger, we describe its properties in § 2.2. We establish the region of the system's parameter space in which the oscillatory dynamics occur by systematically

https://doi.org/10.1017/jfm.2025.10664 Published online by Cambridge University Press

varying the bubble's size and flow rate, and constructing a phase diagram, in § 3.1. The underlying physical mechanism that leads to periodic oscillations is described in § 3.2. Finally, we discuss the significance of our findings and avenues for future work in § 4.

2. Experimental methods

2.1. *Experimental set-up*

The experiments were performed inside a rectangular Hele-Shaw channel (figure 2*a*), which has previously been described comprehensively by Gaillard *et al.* (2021). The channel consisted of two float glass plates that were separated by two parallel sheets of steel shim (figure 2*b*). The channel was approximately $L^* \approx 2$ m long, its width was $W^* = 40.0 \pm 0.1$ mm, and its depth was $H^* = 1.00 \pm 0.01$ mm, which was confirmed by a series of uniformly spaced measurements along the channel's length with a micrometer screw gauge. The channel was filled with silicone oil (Basildon Chemicals Ltd) of dynamic viscosity $\mu = 0.019$ Pa s, density $\rho = 951$ kg m^{-3} and surface tension $\sigma = 21$ mN m^{-1} at the ambient laboratory temperature 21 ± 1 °C. The flow of oil was controlled by two syringe pumps (KD Scientific) that were connected together in parallel with rigid plastic tubes. These withdrawal syringe pumps were linked to the channel outlet and an external oil reservoir with a three-way solenoid valve; this allowed us to control flow into/out of the channel, and to refill the channel prior to experiments. The channel was connected to the atmosphere by a two-way air valve that was situated a short distance downstream of the channel inlet. The syringe pumps and solenoid valves were linked to TTL switches and controlled on a computer with custom-built LabVIEW programs.

We generated a bubble inside the channel by manually injecting air through a small tube that was threaded through the channel inlet and connected to a 25 µl syringe; this method did not allow us to precisely control the bubble's volume. However, the bubble's size was measured precisely using an edge-detection algorithm, and repeat experiments were performed in order to span the required range of bubble sizes. The bubble was propagated to a position downstream of the air valve by withdrawing a small quantity of oil, and aligned approximately with the channel's centreline; this was achieved non-invasively by tilting the channel about its streamwise axis and allowing the bubble to free-rise under buoyancy (figure 2*c*). The channel was returned to its horizontal position, and the experiment was initiated by withdrawing oil at a constant volumetric flow rate Q^* whilst the air valve was open to the atmosphere. The invading finger of air was filmed in top view by an overhead CMOS camera that was mounted onto a motorised translation stage. The camera's observation window was 1760 × 330 pixels, and the camera's frame rate was varied between 12 and 60 frames per second depending on the imposed flow rate. The finger's propagation speed following aggregation with the bubble is not known *a priori*, so the camera's translation speed was manually adjusted until it moved at approximately the same speed as the finger's tip in order to keep it in the camera's field of view throughout the experiments. The air–oil interface was visualised by illuminating the channel from below with a custom-built LED light box; this led to the interface appearing as a darkened contour when viewed from above. However, this technique leads to small uncertainties in our measurements because the interface appears to have a finite thickness of approximately 2 pixels. The contours were detected with a Canny edge-detection algorithm, implemented using a custom-built Python script, which allowed for measurements of the bubble's size, the finger's width and its propagation speed.

We use the channel's half-width $W^*/2$ and the average speed of oil $U_0^* = Q^*/(W^* H^*)$, respectively as our characteristic length and velocity scales in the plane of propagation.

https://doi.org/10.1017/jfm.2025.10664 Published online by Cambridge University Press

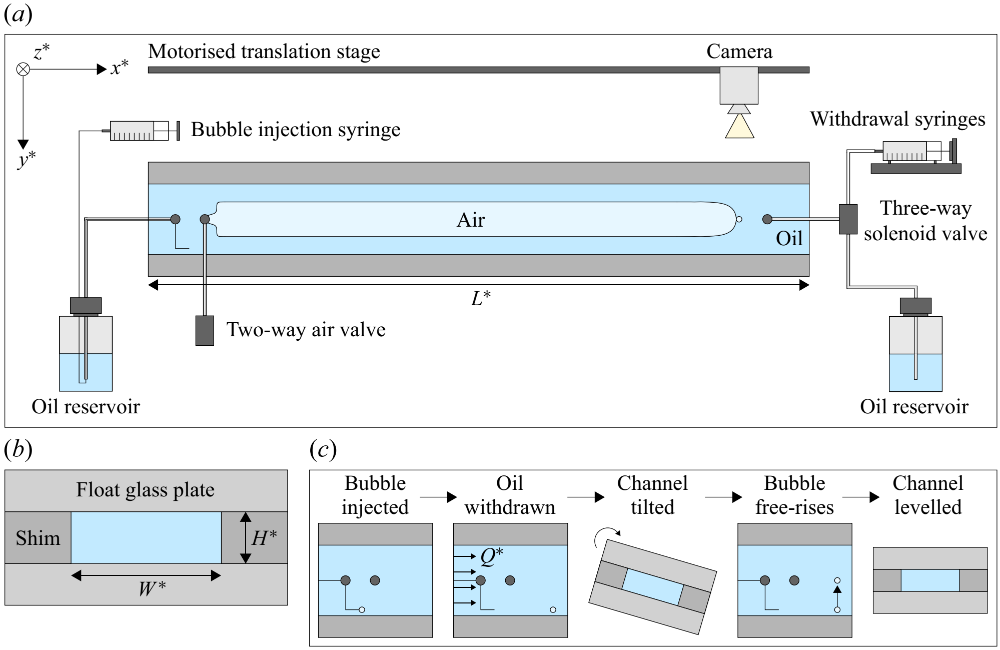

Figure 2. (*a*) The horizontally levelled rectangular Hele-Shaw channel. The channel's width is $W^* = 40.0 \pm 0.1$ mm, and its depth is $H^* = 1.00 \pm 0.01$ mm. The channel outlet is connected to a network of syringe pumps and an external oil reservoir by a three-way solenoid valve. The channel inlet is connected to an external oil reservoir. The experiments are recorded in top view by a steadily translating CMOS camera that is mounted onto a motorised translation stage. (*b*) The channel's cross-section. (*c*) The five-step procedure that is used to generate a centred bubble prior to an experiment.

We use the two-dimensional coordinate system (x, y) to describe the finger, where $x = 2x^*/W^*$ and $y = 2y^*/W^*$ are the dimensionless coordinates spanning the length and width of the channel, respectively. The line $y = 0$ corresponds to the axial centreline of the channel, whilst the channel's side-walls are given by the lines $y = \pm 1$. The dimensionless flow rate is given by $Q = \mu U_0^*/\sigma$, which is a capillary number based on the average speed of the oil, and takes values in the range $0 \leqslant Q \leqslant 0.12$ in our experiments. We determined the finger's speed U^* by calculating the streamwise displacement of its tip across a series of consecutive frames, and its dimensionless speed relative to the mean speed of the surrounding oil is given by $U = U^*/U_0^*$. The capillary number based on the finger's speed is given by $Ca = \mu U^*/\sigma$, and this is related to Q by $Ca = QU$. The bubble's size is parametrised in terms of a dimensionless radius $r = 2\sqrt{A^*/\pi}/W^*$, where A^* is the projected area measured in-flow through image analysis, and we note that this differs from the stationary projected area due to the presence of liquid films around the moving bubble and compressional effects (Gaillard *et al.* 2021).

2.2. *The single, symmetric Saffman–Taylor finger*

Figure 3 shows the variations with dimensionless flow rate $Q = \mu U_0^*/\sigma$ of two quantities that characterise the single, symmetric Saffman–Taylor finger: the fraction of the channel's width occupied by the finger, $\lambda = \lambda^*/W^*$ (figure 3*a*), and the finger's dimensionless speed $U = U^*/U_0^*$ (figure 3*b*). As the flow rate increases, the finger width initially decreases, because the corresponding increase in viscous pressure drop leads to increased curvature of the finger tip, given the finite surface tension. The half-width finger predicted by

https://doi.org/10.1017/jfm.2025.10664 Published online by Cambridge University Press

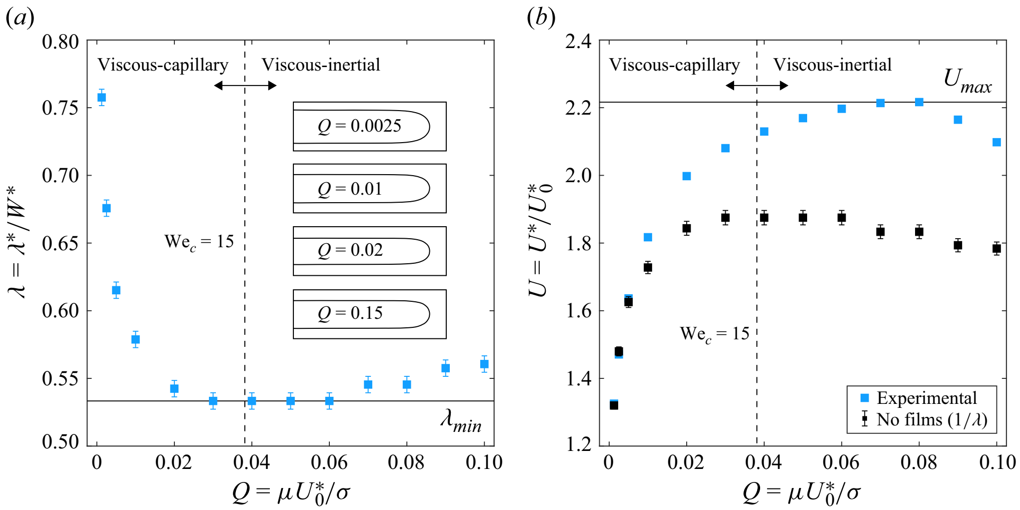

Figure 3. (*a*) The fraction of the channel's width $\lambda = \lambda^*/W^*$ occupied by the Saffman–Taylor finger. (*b*) The dimensionless speed $U = U^*/U_0^*$ as the dimensionless flow rate $Q = \mu U_0^*/\sigma$ varies. The critical value of the modified Weber number $We_c = \rho U_c^{*2} W^*/\sigma = 15$ that was identified by Chevalier *et al.* (2006) is indicated by the dashed vertical line. The channel's width is $W^* = 40.0 \pm 0.1$ mm, and its depth is $H^* = 1.00 \pm 0.01$ mm.

the depth-averaged lubrication model is not observed in our experiments. Instead, the finger width plateaus at a minimum value $\lambda = \lambda_{min} \equiv 0.53$, before increasing slightly. Broadening of the Saffman–Taylor finger was shown by Chevalier *et al.* (2006) to arise from inertial effects, which become significant as the propagation speed increases. They showed that the finger broadens measurably beyond a threshold Weber number $We = \rho U^{*2} W^*/\sigma = 15$, the ratio of inertial to surface tension forces. This threshold, which we indicate with dashed vertical lines in figure 3, delineates the transition between the viscous-capillary and viscous-inertial regimes in our experiment, in which the width of the finger decreases and increases, respectively, with increasing flow rate. However, despite inertial effects influencing the finger width at higher flow rates, we will later present evidence to show that they do not play an important role in the observed oscillatory dynamics.

The finger's dimensionless speed is related to its relative width by mass conservation, yielding the simple relationship $U = 1/\lambda$ in the two-dimensional ($h \rightarrow 0$) limit. For finite h, the relationship between the finger's width and speed is modified by the presence of liquid films situated above and below the finger, arising from the wettability of the liquid with the channel's boundaries. The thickness of these films increases with the capillary number (see figure 4), and the theoretical result of Bretherton (1961) is also shown, although this is known to be accurate only for $Ca \leqslant 10^{-4}$. We have also included least squares fits to the empirical relationships established by Tabeling *et al.* (1987) and Aussillous & Quéré (2000) in figure 4, which are the higher-speed modifications of the Bretherton relationship, both of which exhibit an excellent agreement with our measurements. For small Q, these films are thin, meaning that U is approximately equal to $1/\lambda$. The film thickness grows as Q increases, and the finger effectively propagates into a channel of reduced depth, leading to an increased propagation speed for fixed λ. The increasing film thickness is indicated by the speed of the finger deviating from the film-free prediction ($1/\lambda$) as Q increases. Following the onset of inertial broadening,

https://doi.org/10.1017/jfm.2025.10664 Published online by Cambridge University Press

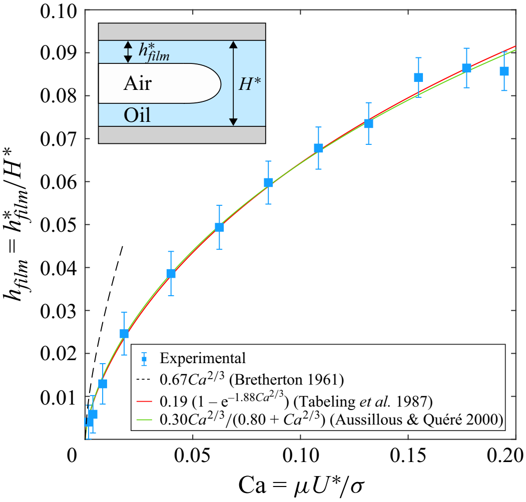

Figure 4. Variation of the dimensionless mean liquid film thickness $h_{film} = h^*_{film}/H^*$ as a function of the capillary number $Ca = \mu U^*/\sigma$. Experimental data are shown with symbols, while red and green solid lines indicate least square fits to the empirical relationships proposed by Tabeling *et al.* (1987) and Aussillous & Quéré (2000), respectively. The analytical prediction by Bretherton (1961), valid for $Ca \to 0$, is shown with a dashed black line. Inset: simplified side view schematic diagram of the liquid films above and below the finger.

the finger's dimensionless speed continues to increase with increasing flow rate because the increasing finger width, which would cause a reduction in speed, is outweighed by the increasing film thickness. However, the converse is true for higher flow rates, as indicated by the decrease in U for flow rates exceeding $Q \geqslant 0.08$; see figure 3.

Throughout this paper, the shapes of aggregate fingers will be compared to those of single fingers, described by established analytical and empirical results. Saffman & Taylor (1958) derived an analytical expression that accurately describes the single finger shapes for $\lambda \leqslant 0.50$. However, as noted by Pitts (1980), these predictions deviate increasingly from the experimental shapes as the width of the finger increases beyond $\lambda = 0.50$. To address this discrepancy, Pitts used an empirical relationship for the local curvature along the interface of the finger, leading to a set of modified finger shapes. A closed-form expression for the shape of a finger in the xy-plane with relative width $\lambda = \lambda^*/W^*$ that combines these two results is given by

$$x(y;\,\lambda) = \frac{F(\lambda)}{\pi} \ln\left[\frac{1 + \cos(\pi y/\lambda)}{2}\right], \tag{2.1}$$

where $(x = 2x^*/W^*,\ y = 2y^*/W^*)$ are the dimensionless coordinates of the interface, and the origin $(x,\ y) = (0,\ 0)$ is situated at the finger's tip. The only difference between the Saffman–Taylor and Pitts expressions is the pre-factor to the logarithm, given by $F(\lambda) = (1 - \lambda)$ for $\lambda \leqslant 0.50$, and $F(\lambda) = \lambda$ for $\lambda > 0.50$.

The comparison between the experimental observations and the predicted interface shapes from both expressions is shown in figure 5 for three representative finger widths. Here, the blue-coloured contours correspond to the shapes derived from the Saffman–Taylor expression, whilst the red-coloured contours correspond to those obtained from the Pitts expression. For smaller values of λ, the Saffman–Taylor expression provides a noticeably closer match to the experimental profiles. However, for larger values of λ, the converse is true. Note that we cannot compare the predicted interface shapes to

https://doi.org/10.1017/jfm.2025.10664 Published online by Cambridge University Press

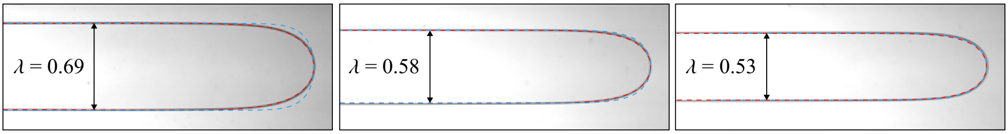

Figure 5. The experimental finger shapes, overlaid with the shapes predicted by Saffman & Taylor (1958) (blue) and Pitts (1980) (red) for three different finger widths.

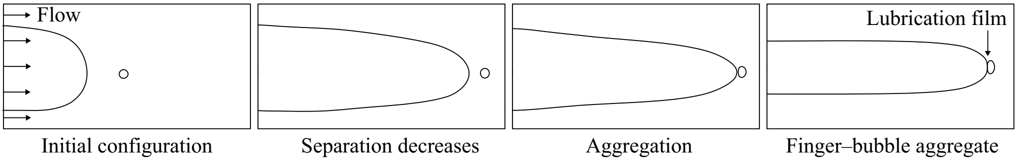

Figure 6. The general behaviour of the system shortly after the finger is formed by withdrawing the oil at a constant flux from the opposing end of the channel whilst the air valve is open to the atmosphere. A lubrication film prevents the bubble and finger from immediately coalescing.

experimental fingers for $\lambda < 0.50$ in this section, because the experimental fingers do not attain such narrow widths in any circumstance. Nevertheless, the shapes predicted by Saffman & Taylor (1958) will become particularly relevant in the subsequent analysis, where we consider perturbed fingers that can access this range of λ.

3. Results

3.1. *Phase diagram of the finger's long-term behaviour*

The time sequence in figure 6 shows the typical dynamics shortly after the finger is formed. The finger initially catches up to the bubble because its propagation speed is faster, and this leads to their aggregation. However, the coalescence between the bubble and finger is delayed because they are separated by a thin liquid film. For flow rates smaller than $Q < 0.02$, the liquid film ruptures shortly after aggregation, which leads to coalescence into a single finger; see movie 1 in the supplementary materials available at https://doi.org/10.1017/jfm.2025.10664. However, the liquid film persists throughout the entirety of the experiment for higher flow rates, irrespective of the bubble's size. The bubble, which deforms as the finger pushes up against its rear, replaces the finger's tip, and the system evolves until the finger–bubble aggregate assumes either a steady, periodic, or continuously evolving mode of propagation. We have not pursued a detailed investigation of the initial conditions required to achieve aggregation, but our experiments show that very small bubbles act as tracer particles, and are swept past the finger tip, whilst bubbles that are sufficiently large will always get attracted to the centreline of the channel. It is likely, therefore, that the region in which the bubble is attracted towards the tip scales with bubble size for small bubbles, and reaches the width of the entire channel for sufficiently large bubbles.

The two-dimensional phase diagram in figure 7, which contains the results of over two hundred experiments, characterises the influence of the bubble's dimensionless size $r = 2\sqrt{A^*/\pi}/W^*$ (horizontal axis) and dimensionless flow rate $Q = \mu U_0^*/\sigma$ (vertical axis) on the finger's long-term behaviour. We identified five distinct modes of propagation over the explored parameter space, occurring in two distinct simply connected regions; see movies 2–7 in the supplementary material for illustrative examples.

https://doi.org/10.1017/jfm.2025.10664 Published online by Cambridge University Press

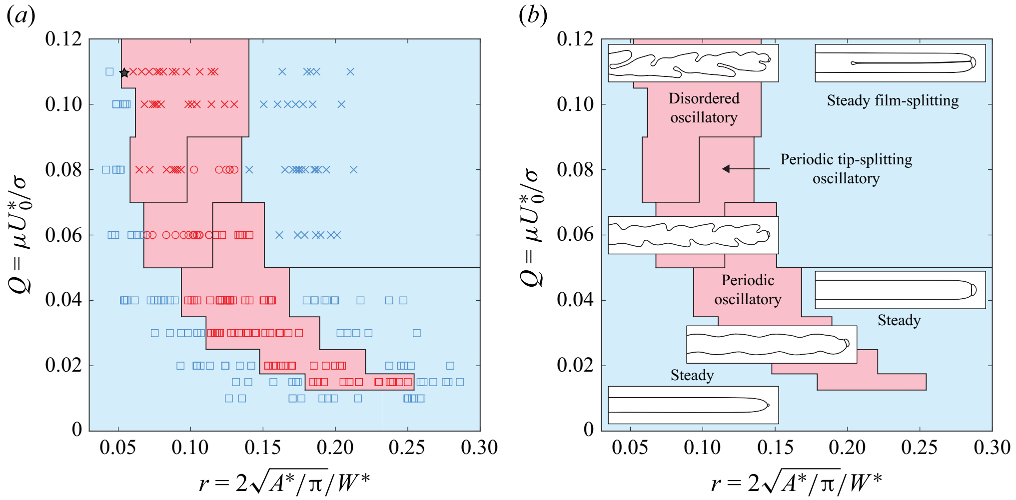

Figure 7. (*a*) Two-dimensional phase diagram characterising how the bubble's dimensionless size $r = 2\sqrt{A^*/\pi}/W^*$ (horizontal axis) and dimensionless flow rate $Q = \mu U_0^*/\sigma$ (vertical axis) influence the finger's long-term behaviour. We were unable to obtain measurements for $r < 0.05$. The data markers are used to indicate different long-term behaviours, and the background colours indicate whether the finger tip propagates steadily (blue) or oscillates (red). The black star marker indicates where a single occurrence of a pulsating mode was observed, discussed further in § 4. The piecewise-linear solid lines are the approximate boundaries between regions of different long-term behaviours. (*b*) Reproduction of the phase diagram with the data markers removed. The overlaid images are examples of the typical finger shapes; see movies 2–7 in the supplementary material.

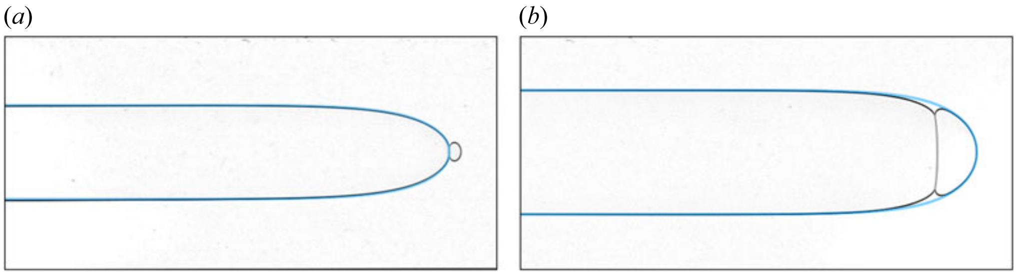

Aggregate finger matches conventional finger profile
(narrower width) non-inclusive of bubble

Aggregate finger matches conventional finger
(same width) inclusive of bubble

Figure 8. Representative examples of the two ways in which the single finger shapes, represented by the blue-coloured contours, appear in the aggregate finger shapes for steadily propagating fingers. (*a*) The portion of the aggregate non-inclusive of the bubble matches the equivalent-width, single-finger shape. The relative finger width is $\lambda = 0.40$. (*b*) The entirety of the aggregate matches the equivalent-width, single-finger shape. The relative finger width is $\lambda = 0.53$. The dimensionless flow rate is $Q = \mu U_0^*/\sigma = 0.04$ in both cases.

3.1.1. *Steadily propagating fingers*

For flow rates below $Q \leqslant 0.0125 \pm 0.0005$, the finger–bubble aggregate propagates steadily for all bubble sizes. However, for higher flow rates, the aggregate only propagates steadily for sufficiently small or sufficiently large bubbles.

A characteristic property of the steadily propagating finger–bubble aggregate is that its overall shape closely resembles a single finger of the same width, as described by (2.1). However, this resemblance manifests in two different ways, depending on the size of the bubble; see figure 8 for illustrative examples. For small bubbles, the aggregate finger

https://doi.org/10.1017/jfm.2025.10664 Published online by Cambridge University Press

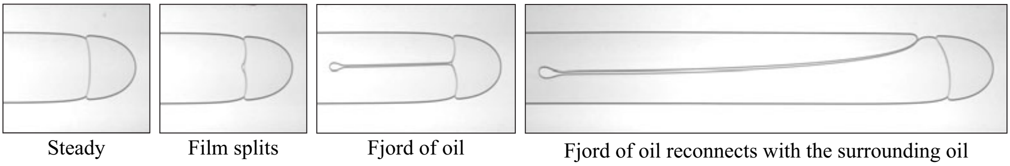

Figure 9. The splitting of the liquid film between the bubble and finger that occurs for steadily propagating fingers with sufficiently large bubbles at high flow rates. The splitting of the liquid film leads to the development of a narrow fjord of liquid inside the finger that progressively bends towards one of its sides. The relative width of the finger is $\lambda = 0.53$, and its dimensionless speed is $U = 2.19$. The dimensionless flow rate is $Q = \mu U_0^*/\sigma = 0.06$.

is narrower than the equivalent single finger, and Couder *et al.* (1986) showed that the portion of the aggregate excluding the bubble is well described by the equivalent-width, single-finger shape. Hence in this regime, the bubble appears to be locally perturbing the flow field in front of the finger tip. We hypothesise that the mechanism by which the bubble causes the finger narrowing is similar to how a rigid disk placed in front of the finger tip can lead to narrowing, by locally reducing the fluid pressure and consequently increasing the propagation speed and the curvature of the finger tip (Thomé *et al.* 1990). The resemblance to the single finger is different for larger bubbles, for which it is the entirety of the aggregate that is well described by the equivalent-width, single-finger shape. In this regime, the bubble is large enough to conform to the shape of the single finger tip, thereby becoming part of the overall finger shape. The observations indicate that despite the presence of the bubble at its tip, the steadily propagating aggregate finger is clearly subject to the same mechanism that governs the overall shape of single fingers. Note that the finger–bubble aggregates do not appear to be well described by the available exact zero-surface-tension solutions for fingers with bubbles at their tips (Vasconcelos 1999, 2000, 2015). After matching finger widths and bubble sizes, the finger tips and bubbles are both wider in the experiments compared to the exact solutions, indicating the importance of surface tension in the experimental system. Given the lack of agreement, we choose not to pursue this comparison further.

The time sequence in figure 9 shows an effect that occurs for steadily propagating aggregates for flow rates exceeding $Q \geqslant 0.05 \pm 0.01$. Here, the liquid film that separates the bubble and finger repeatedly splits, leading to the growth of a narrow fjord of liquid inside the finger. We have continued to refer to these fingers as steady because we are referring to the motion of the tip, which remains uninfluenced by the splitting of the film. The liquid fjord progressively bends towards one side of the finger, before connecting with the surrounding liquid as the finger advances. The splitting of the liquid film occurs irregularly, and its initial location varies, indicating that this effect may be driven by perturbations. The fjord length depends on how symmetrically the liquid film splits, as longer fjords develop if the splitting begins close to the centre of the film at $y = 0$, whilst shorter fjords develop if the splitting occurs in off-centre positions (Kopf-Sill & Homsy 1988; Lajeunesse & Couder 2000). We have not yet found an explanation for why this splitting occurs, but the liquid inside the fjord appears to originate from the liquid films that are left behind by the finger on the upper and lower channel boundaries. The interface between the bubble and finger is approximately flat, which suggests that the splitting may arise from a modification of the Saffman–Taylor instability, but the observed wavelength is shorter than the theoretical value $\pi\, Ca^{-1/2}\, H^*$ (Saffman & Taylor 1958).

https://doi.org/10.1017/jfm.2025.10664 Published online by Cambridge University Press

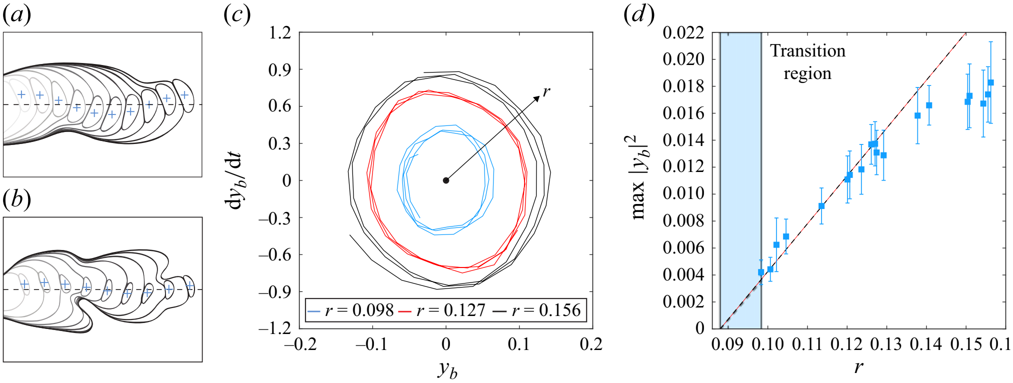

Figure 10. (*a*) Composite image of a periodic oscillation over a single cycle. The bubble's size is $r = 0.156$, and the dimensionless flow rate is $Q = \mu U_0^*/\sigma = 0.04$. (*b*) Composite image of a periodic oscillation including tip-splitting over a single cycle. The blue-coloured markers indicate the positions of the bubble centroid. The bubble's size is $r = 0.102$, and the dimensionless flow rate is $Q = \mu U_0^*/\sigma = 0.08$. (*c*) Two-dimensional phase plane portrait of the finger's trajectories in the $(y_b, \mathrm{d}y_b/\mathrm{d}t)$ projection, where y_b is the lateral coordinate of the bubble's centroid, for three different bubble sizes. (*d*) Variation of the oscillation amplitude max $|y_b|^2$ as a function of the bubble size r. The dimensionless flow rate is $Q = \mu U_0^*/\sigma = 0.04$.

3.1.2. *Oscillating fingers*

For flow rates exceeding $Q > 0.0125 \pm 0.0005$, a region of oscillatory fingers emerges for intermediately sized bubbles, thereby separating two intervals of bubble sizes that yield steadily propagating fingers. The region of oscillations is approximately constant in width for the range of flow rates investigated, but shifts to smaller bubble sizes as the flow rate increases, suggesting a connection between the bubble size and single-finger width because this also initially decreases with increasing flow rate; see figure 3. We observed three different types of oscillation, which become more complex as the flow rate increases.

(i) For $Q \leqslant 0.05 \pm 0.01$, the finger's tip periodically oscillates laterally about the channel's centreline $y = 0$ for all bubbles in the red-coloured region of the phase diagram (figure 7), leading to the development of regular wave-like fingering patterns; see figure 10(*a*).
(ii) For $0.05 \leqslant Q \leqslant 0.09$, the periodic oscillations are accompanied by tip-splitting for a range of bubble sizes, leading to the development of increasingly complex patterns; see figure 10(*b*).
(iii) For $Q > 0.09 \pm 0.01$, periodic oscillations are replaced by disordered dynamics, characterised by a seemingly random meandering of the finger's tip as it oscillates laterally; see figures 11(*a*,*b*). The disordered dynamics first appear for smaller bubbles in the red-coloured region of (figure 7) at $Q = 0.07 \pm 0.01$, but they occur for all bubbles in the red-coloured region for $Q \geqslant 0.09 \pm 0.01$.

We have projected the trajectories of the bubble's centroid at $Q = \mu U_0^*/\sigma = 0.04$ onto the two-dimensional $(y_b, \mathrm{d}y_b/\mathrm{d}t)$ plane in figure 10(*c*). Although we are only showing these measurements for one particular flow rate, the phase portrait is qualitatively representative of all flow rates in which the steadily propagating finger destabilises into stable periodic states. The steadily propagating fingers are stable fixed points lying at the origin, whilst the oscillations correspond to closed loops centred about the origin in this particular projection. Beyond onset, the squared amplitude of the periodic orbits increases

https://doi.org/10.1017/jfm.2025.10664 Published online by Cambridge University Press

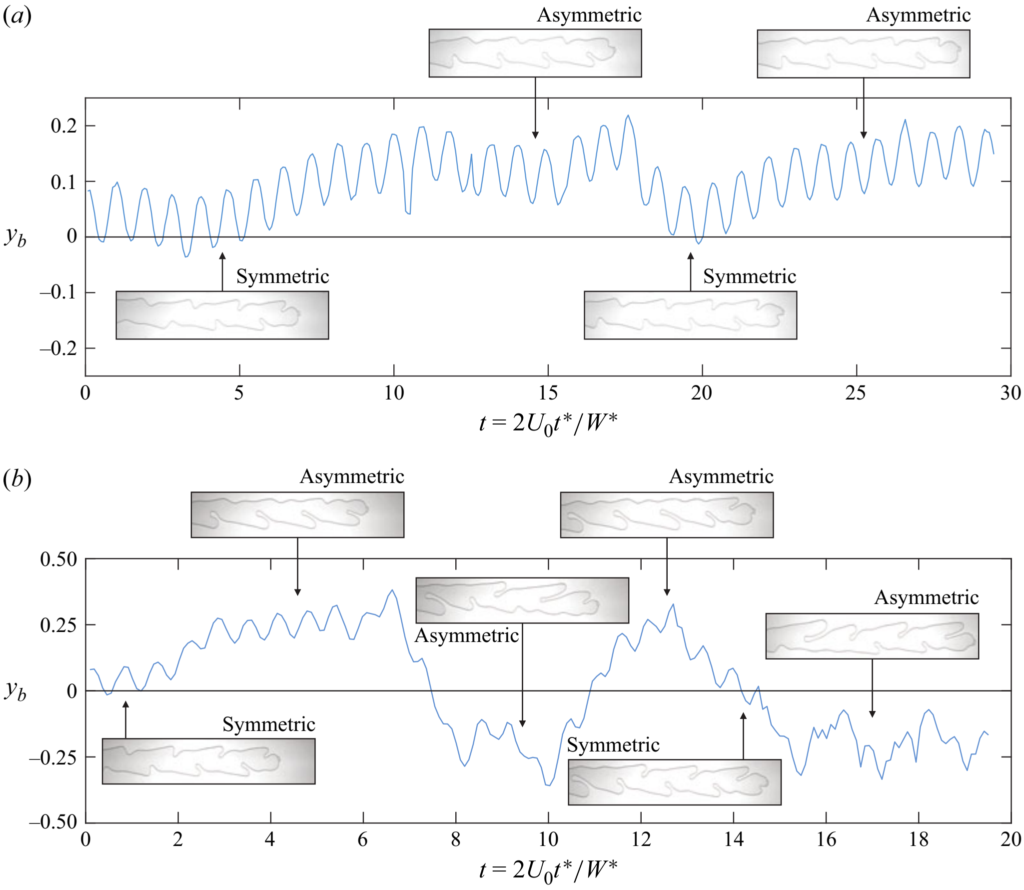

Figure 11. (*a*) Time evolution of the y-coordinate of the bubble's centroid where the bubble's size is $r = 0.065$ and the dimensionless flow rate is $Q = \mu U_0^*/\sigma = 0.08$. (*b*) Time evolution of the y-coordinate of the bubble's centroid where the bubble's size is $r = 0.067$ and the dimensionless flow rate is $Q = \mu U_0^*/\sigma = 0.10$. In both plots, the insets show the patterns left behind by the finger at various points in time.

approximately linearly as the bubble grows in size (see figure 10*d*), which is dynamically consistent with a supercritical Hopf bifurcation.

The oscillation period is found to increase with bubble size at fixed flow rate. For the range of investigated flow rates over which stable oscillations occur, this increase is approximately 20 % across the interval of bubble sizes. The increasing period can be attributed to the increasing oscillation amplitude, meaning that the bubble gets further away from the channel centreline and therefore takes longer to return there each cycle. Similar behaviour is observed as the flow rate increases for a fixed bubble size, which is attributed to the increasing deformability of the bubble that drives it further from the channel centreline.

For the highest flow rates, the irregular patterns that are left behind by the disordered finger are qualitatively reminiscent of those observed following the destabilisation of the single finger at sufficiently large values of the driving parameter (Tabeling *et al.* 1987). Furthermore, the continuously evolving dynamics in this region are accompanied by high sensitivity, because repeat experiments with similar bubble sizes lead to strikingly different evolutions.

https://doi.org/10.1017/jfm.2025.10664 Published online by Cambridge University Press

The time evolution of y_b shown in figure 11(a) is an example of the disordered dynamics at $Q = \mu U_0^*/\sigma = 0.08$. Here, the tip of the finger oscillates with a well-defined period, but the oscillations are no longer centred about $y = 0$. The complex finger tip oscillations do have an underlying structure, however, and appear to drift regularly between a centred mode and an off-centred mode.

The finger's dynamics become increasingly erratic at higher flow rates, leading to the generation of complex patterns. The time evolution of y_b in figure 11(b) is an example of the disordered dynamics at $Q = \mu U_0^*/\sigma = 0.10$. Here, the time evolution features abrupt switches in addition to the slower drifts that were described previously, between different types of oscillations. Note that for these relatively high-speed experiments, the available time resolution does not allow sufficiently accurate determination of the time derivatives to construct a meaningful phase diagram.

The two time evolutions shown in figure 11, although different in their complexity, are both dynamically consistent with the transient exploration of multiple, unstable periodic states. The centred oscillations are similar to the original periodic states, but they are no longer stable, and the asymmetric oscillations appear to be new periodic states that were not observed at lower flow rates. In figure 11(a), the behaviour is consistent with the interaction of two periodic states with different frequencies; at higher flow rates, figure 11(b), the behaviour is consistent with interaction of more than two periodic states with different frequencies. In the latter case, the development of large side-tips on the side of the finger furthest from the neighbouring side-wall in the off-centred oscillations provides a physical mechanism to keep the finger off-centre, because they will tend to impede the finger's movement towards the channel's centreline. The off-centred oscillations about $y < 0$ are irregular, unlike those about $y > 0$, which are nearly perfectly periodic, and we speculate that this behaviour is driven by asymmetries, such as the unavoidable bias in the levelling of the channel, in our experiments.

3.1.3. *Finger width and propagation speed*

In this subsubsection, we compare the width and propagation speed of the aggregate finger to the equivalent single finger as the size of the bubble varies. The two plots in figure 12 show the two dimensionless properties as functions of the bubble size at $Q = \mu U_0^*/\sigma = 0.04$, and although we are only showing these for one particular flow rate, we note that they are qualitatively representative of all investigated flow rates.

As the size of the bubble increases, the width of the finger increases, and the speed of the finger decreases. Here, the overlaid fits show that the two quantities are inversely proportional, with $U = 1.13/\lambda$. The broadening of the finger occurs because the curvature that is imposed by the bubble at the finger tip decreases as the size of the bubble increases; a smaller curvature decreases the surface-tension-induced pressure jump across the tip of the bubble, thereby increasing the local fluid pressure in this region (Couder *et al.* 1986). Consequently, the overall fluid pressure gradient decreases, and since the speed of the finger is proportional to this gradient, the system selects a slower and therefore broader finger.

For sufficiently large bubbles, the width and speed of the finger remain approximately constant, with values corresponding to those of a single finger at the imposed flow rate. Hence the behaviour in the large-r limit is that the aggregate effectively behaves the same as a single finger, which is consistent with the shape of the bubble conforming to the shape of the single-finger tip; see figure 8.

The width of the finger at the first transition point is significantly narrower than the equivalent single finger. Following the onset of oscillations, the lateral motion of the finger tip appears to have no effect on its mean propagation speed, which continues to decrease smoothly without discontinuity as the size of the bubble increases. Based on this

https://doi.org/10.1017/jfm.2025.10664 Published online by Cambridge University Press

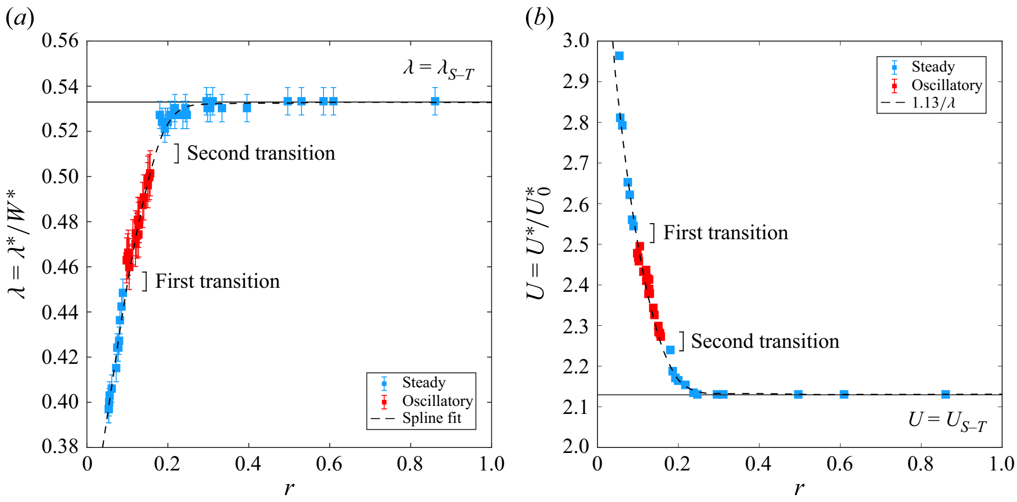

Figure 12. Variation of the finger's (*a*) relative width $\lambda = \lambda^*/W^*$ and (*b*) dimensionless speed $U = U^*/U_0^*$ as functions of the bubble size r at $Q = \mu U_0^*/\sigma = 0.04$. λ_{S-T} and U_{S-T} denote, respectively, the finger width and finger velocity of a Saffman-Taylor finger in the absence of a tip-bubble. The blue data markers correspond to steadily propagating fingers, and red data markers correspond to oscillatory fingers. The width of steady fingers was determined from direct measurement, whilst the mean width of oscillatory fingers was determined indirectly from mass conservation by measuring the finger speed, and interpolating the thickness of the deposited oil films. The error bars in (*a*) arise from the apparent thickness of the air–oil interface, whilst they have been omitted in (*b*) because they are smaller than the data markers. The black dashed line indicates the curve $1.13/\lambda$, which was obtained from a spline fit through the experimental data points in (*a*) for λ.

insight, and given the consistency of our previous observations with the oscillations arising through a supercritical Hopf bifurcation, we infer that the width of the finger is governed primarily by the underlying unstable steadily propagating state from which the stable limit cycle emerges. Once the width of the finger is approximately equal to that of a single finger at the imposed flow rate, the oscillations stop, and the finger returns to steady propagation. The relevance of this observation will become apparent in § 3.2.2, when describing the physical mechanism underlying this transition.

As described previously, the thickness of the liquid films is determined by the capillary number, which varies in the range $0.09 \leqslant Ca \leqslant 0.12$ over this range of finger speeds. Within this range, the film thickness varies in the range $0.06 \leqslant h \leqslant 0.07$; see figure 4. Hence the finger's thickness does not vary significantly, meaning that three-dimensional effects are not expected to play a significant role. The finding is reinforced by the inversely proportional relationship between the width of the finger and its propagation speed, thereby suggesting that the perturbation applied at the tip of the finger by the bubble is essentially a two-dimensional effect. Hence we can simplify our proceeding analysis by disregarding the z-direction, and only considering the finger shapes in the xy-plane.

3.2. *Transitions to oscillations*

The two transitions between steady and oscillatory propagation shown in figure 7 are well described by smooth r^α relationships over the investigated range of parameters, as indicated by the linear relationships between the values of r and Q at which they occur on log-log axes in figure 13. These relationships indicate that the critical bubble radius depends on the geometry of the finger. In the absence of inertia, $\lambda \sim Ca^{-2/3}$ near the limiting finger width (Couder *et al.* 1986). Hence $Ca = UQ \sim \lambda^{-3/2}$, and if we assume that the finger width scales with bubble radius, $\lambda \sim r$, then $UQ \sim r^{-3/2}$. If U remains

https://doi.org/10.1017/jfm.2025.10664 Published online by Cambridge University Press

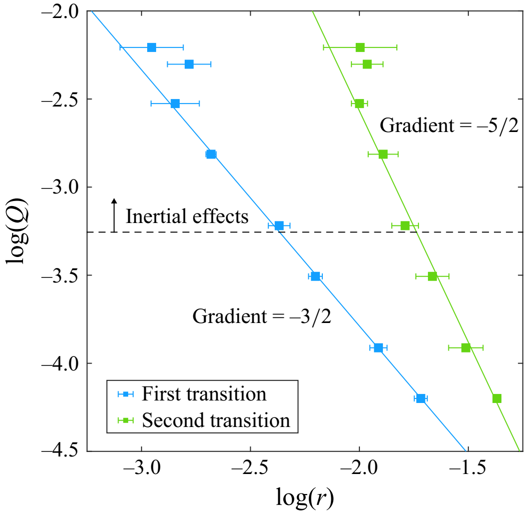

Figure 13. Log-log plot of the two transition points in the (r, Q) plane. The experimental measurements are well described by linear least squares regression fits. The horizontal dashed line coincides with the value of Q where the critical Weber number is exceeded for the single Saffman–Taylor finger, indicating that the finger is subject to broadening due to inertial effects above it.

approximately constant, then the system is driven by the finger speed, and we obtain the scaling $Q \sim r^{-3/2}$, which describes the first transition from steady to oscillatory fingers. Alternatively, if the system is driven by the bubble speed, then $U \sim r$, and we obtain the scaling $Q \sim r^{-5/2}$, which describes the second transition where the oscillations stop and the finger returns to steady propagation. The scaling $U \sim r$ can be found by balancing the viscous and capillary pressure drops over an isolated bubble (Booth *et al.* 2025). We note that these scalings do not explain what sets the critical bubble radius for each transition, but they do indicate how such a critical radius varies with flow rate.

The observed deviation from these scalings at high values of Q coincides with the decrease in finger propagation speed due to inertial effects; see § 2.2. Hence, although inertial effects cannot be neglected for sufficiently high flow rates, they do not appear to play a significant role in either of the transitions to oscillatory behaviour over the investigated range of parameters, indicating that the mechanism for oscillations is not inertially driven.

The two sets of images in figure 14 show the limiting steadily propagating finger shapes bounding either side of the region of oscillations for different flow rates. We conjecture that the key to understanding the transition mechanisms lies in identifying common geometrical properties linking these two sets of steadily propagating finger shapes, and we will now examine how the steadily propagating finger and bubble shapes change leading up to the onset of oscillations.

3.2.1. *First transition*

The first transition is best understood by starting with the smallest bubbles and progressively increasing the size of the bubble until the finger oscillates. The sequence of images in figure 15(*a*) shows the steadily propagating fingers, alongside enlargements of the corresponding bubble shapes as the size of the bubble increases at $Q = \mu U_0^*/\sigma = 0.04$. The overlaid blue-coloured contours are the equivalent-width single-finger shapes, which, as described in § 3.1, match the portion of the aggregate non-inclusive of the bubble

https://doi.org/10.1017/jfm.2025.10664 Published online by Cambridge University Press

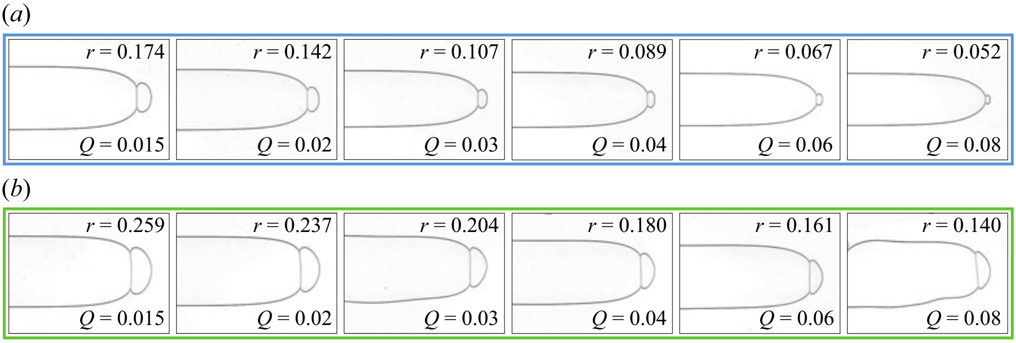

Figure 14. The limiting steadily propagating finger shapes on both sides of the region of oscillations at different flow rates. (*a*) Images correspond to the largest bubbles that resulted in steadily propagating fingers prior to the first transition. (*b*) Images correspond to the smallest bubbles that resulted in steadily propagating fingers after the second transition. The fingers wobble slightly at high flow rates because the liquid film that separates the bubble and finger repeatedly splits.

remarkably well in all cases. Despite the significant change in the size of the bubble, the width of the finger remains approximately constant ($0.40 \leqslant \lambda \leqslant 0.45$) over the investigated range of bubble sizes.

The shapes of the smallest bubbles are dominated by surface tension, and are near circular. The larger bubbles are influenced by viscous forces, and they adopt kidney-bean-like shapes. These shapes are notably different from the typical bubble shapes in Hele-Shaw cells, which tend to elongate in the direction of motion in order to reduce their resistance in viscous-dominated flow regimes; see Monnet *et al.* (2022). The observed lateral elongation is a consequence of the presence of the finger, which impedes the bubble's ability to elongate in the direction of motion.

The front of the bubble is approximately uniformly curved, which means that we can obtain the dimensionless curvature of its tip $\kappa_b = \kappa_b^* W^*/2$ by measuring the radius $r_b = 2r_b^*/W^*$ of its osculating circle; see the overlaid circles in figure 15(*b*). The curvature at the equivalent-width, single-finger tip κ_f is found by measuring the finger width and using (2.1) in the formula for the local curvature $\kappa = x''/(1 + x'^2)^{3/2}$, which simplifies to

$$\kappa_f = \left| \frac{(\lambda - 1)\pi}{2\lambda^2} \right| \tag{3.1}$$

when evaluated at the tip. The two curvatures are plotted as functions of the bubble's size in figure 16(*a*), and the coloured 'transition region' represents the interval of bubble sizes between the final steadily propagating and first oscillatory data points. The curvature of the bubble's tip is initially higher than that of the finger's tip, and they both decrease as the bubble increases in size. The rates at which the two curvatures decrease differ significantly, leading to a sharp decrease in the difference between them, until they converge at the onset of oscillations. Further time-dependent measurements of the two curvatures in experiments where the finger oscillates are consistent with this observation.

When varying the flow rate, we consistently observed that the curvature of the bubble's tip converges towards that of the finger region as the bubble's size increases. The difference between the two curvatures is plotted in figure 16(*b*) as a function of the bubble's size for different flow rates, where the transition regions are represented by the corresponding coloured bands. Hence our results indicate that equality between the two curvatures is the limiting geometrical configuration that drives the first transition between steady and oscillatory fingers.

https://doi.org/10.1017/jfm.2025.10664 Published online by Cambridge University Press

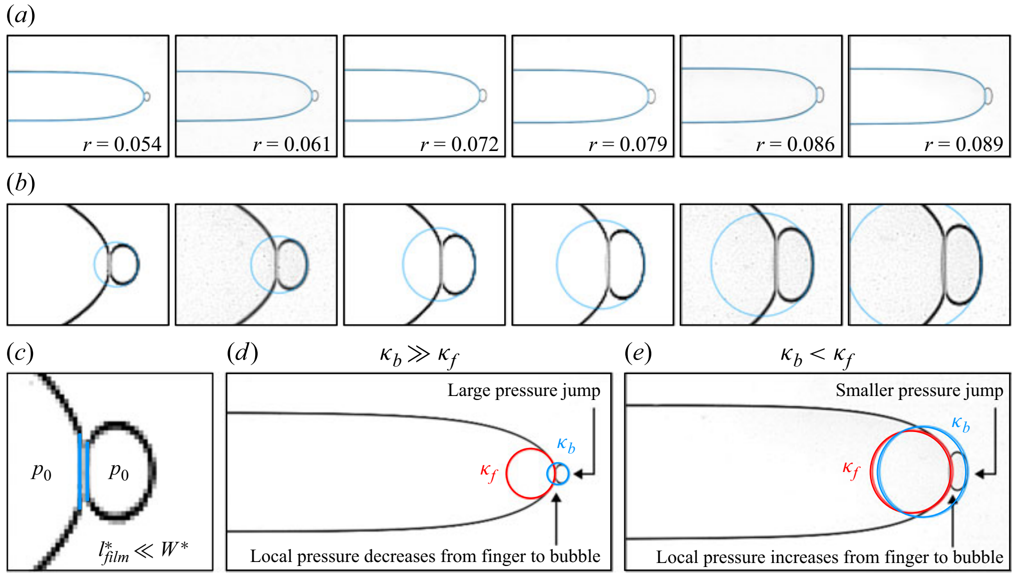

Figure 15. The shapes of the steadily propagating fingers as the bubble's size increases towards the transition point at $Q = \mu U_0^*/\sigma = 0.04$. (*a*) Images show the finger's overall shape. (*b*) Images are zoomed in on the corresponding bubble's shape. The liquid film that separates the bubble and finger is straight within experimental resolution in all cases. The overlaid blue-coloured contours in (*a*) correspond to the equivalent-width, single-finger shapes, whilst the overlaid blue-coloured circles in (*b*) are the osculating circles fitted to the bubble's tip. (*c*) The liquid film between the bubble and finger is straight and has negligible thickness. (*d*,*e*) The variation of the interface's curvature in the vicinity of the aggregate's tip. The regions of low curvature correspond to regions of high liquid pressure, and vice versa. The coloured circles indicate the osculating circles used to determine the curvature of the bubble tip, κ_b: (*d*) example in which the curvature of the bubble's tip is higher than the finger tip; (*e*) example in which the curvature of the bubble's tip is lower than the finger tip.

As described previously, the thicknesses of the liquid films above and below the finger are approximately constant, meaning that the interface curvature in the out-of-plane direction is also approximately constant. Hence changes in fluid pressure can be inferred from the curvature of the interfaces in the xy-plane. We note that the interfaces in the near-contact region between finger and bubble are approximately flat; see figure 15. Hence the surface-tension-induced pressure jump is negligible, meaning that the bubble pressure is approximately the same as the finger pressure.

For steadily propagating aggregates, the maximum curvature of the interface, and therefore the minimum fluid pressure adjacent to the interfaces, is at the tip of the bubble. The enhanced pressure minimum in the vicinity of the finger's tip for narrower fingers may be why Couder *et al.* (1986) found that they destabilise at significantly higher values of the driving parameter $(1/B)$ compared to that for half-width fingers.

Once the finger and bubble tip curvatures are the same, there is no longer an axial pressure gradient along the bubble, and it becomes susceptible to lateral perturbations. If displaced laterally, then both a sufficiently large isolated bubble and the finger will return to the channel's centreline, but they will do so on different time scales. We conjecture that this difference in restoral time scales is what allows sustained oscillations to develop in the aggregate system. Figure 10 shows that the laterally displaced bubble's shape adjusts to drive it back towards the channel centreline, but the bubble is then carried past the centreline by the restoring motion of the finger tip, and the process begins again.

https://doi.org/10.1017/jfm.2025.10664 Published online by Cambridge University Press

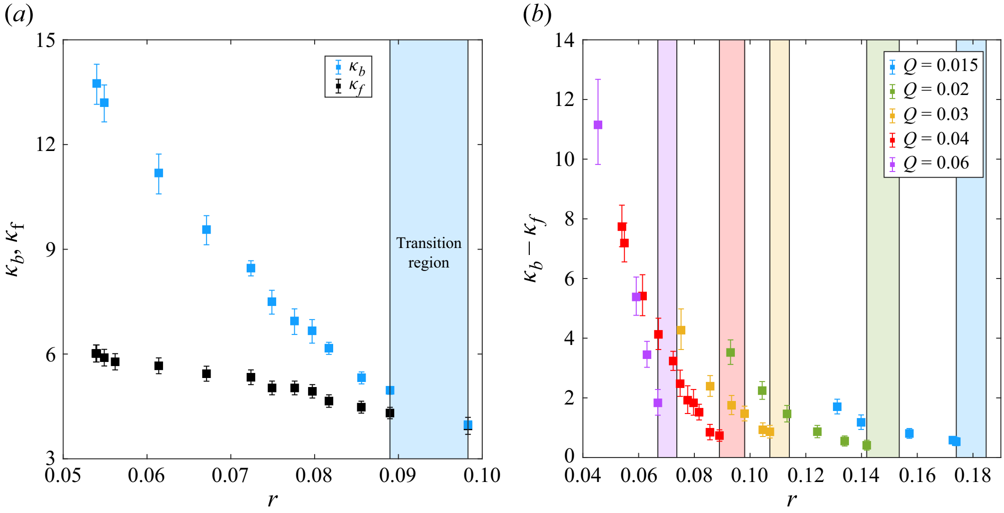

Figure 16. (*a*) Variation of the bubble's tip curvature and the equivalent-width Saffman–Taylor finger's tip curvature as functions of the bubble's size r at $Q = \mu U_0^*/\sigma = 0.04$. The blue-coloured 'transition region' represents the range of bubble sizes between the final steadily propagating and first oscillatory data points. (*b*) Variation of the difference between the curvatures of the bubble's tip and finger's tip as functions of the bubble's size r at five different flow rates. The transition regions are indicated by the corresponding coloured bands of bubble sizes. The error bars in both plots arise from the apparent thickness of the air–liquid interface in the captured frames.

If the bubble is small, then it does not deform; and without the presence of the finger, it would not return to the channel's centreline after lateral displacement. The lack of an independent restoral mechanism for the bubble ensures the stability of the narrowed-finger state because the bubble passively follows the finger's restoral mechanism. This argument is supported by the scalings discussed in § 3.2, which reveal that the system is driven by the finger at the first transition.

3.2.2. *Second transition*

The second transition is best understood by starting with the largest bubbles and progressively decreasing the size of the bubble until the finger oscillates; see figure 17. In this regime, each of the fingers is approximately the same width as the equivalent single finger, and the bubbles are all large enough for their shapes to conform to the single-finger tip shape. Hence the bubble's restoral time scale will be approximately the same as that of the finger, and there is no longer a mechanism for sustained oscillations. In other words, this transition can be understood as the intersection of the two restoral time scales. Again, this argument is supported by the previously discussed scalings, which indicate that the system is driven by the bubble (acting as the finger tip) at the second transition.

For the largest bubbles, the viscous pressure drop associated with the equivalent single propagating finger takes place over the length of the bubble; see figure 18 for an illustrative example. As the bubble size decreases, more of the viscous pressure drop takes place along the finger, and the tip curvature increases accordingly. Based on figure 17, it appears as though the limiting configuration in this regime is the one in which the finger–bubble interface region is approximately flat. Note that the bubble in the limiting configuration is not large enough to act as a single finger in isolation, and it is only the additional deformation caused by interaction with the finger that enables the bubble to conform to the single-finger tip shape. Hence the oscillations begin when the bubble is sufficiently small

https://doi.org/10.1017/jfm.2025.10664 Published online by Cambridge University Press

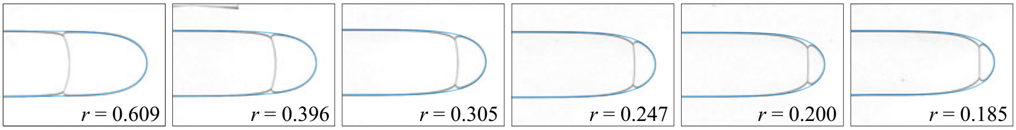

Figure 17. The steadily propagating finger shapes as the bubble's size decreases towards the second transition point at $Q = \mu U_0^*/\sigma = 0.04$. The finger's width is approximately constant. The curvature of the liquid film that separates the bubble and finger decreases as the bubble's size decreases. The overlaid blue-coloured contours correspond to the equivalent-width, single-finger shapes.

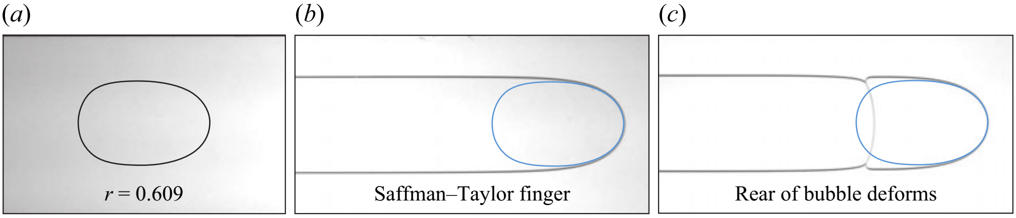

Figure 18. (*a*) A steadily propagating bubble of size $r = 0.609$ at dimensionless flow rate $Q = \mu U_0^*/\sigma = 0.04$. (*b*) The bubble overlaid with the tip of the Saffman–Taylor finger. (*c*) The bubble overlaid with the steadily propagating finger, showing how the rear of the bubble deforms.

such that it cannot conform to the single-finger tip shape, and its restoral time scale differs from that of the finger. However, precisely what sets this threshold is unclear.

4. Discussion

We have investigated experimentally the behaviour of Saffman–Taylor fingers whose tips have been perturbed by bubbles. The experiments serve as an extension to those previously carried out by Couder *et al.* (1986), who explored the anomalous selection of steadily propagating narrow fingers. The authors showed preliminary experiments of the anomalous fingers destabilising into periodic states, yet provided no physical explanation for why this behaviour occurs. We are interested in periodic fingering dynamics because we hypothesise that unstable periodic states are fundamental to the propensity of Saffman–Taylor fingers to exhibit disordered dynamics (Park & Homsy 1985).

The perturbed fingers exhibit a multitude of different long-term behaviours over the investigated range of parameters. We constructed a phase diagram, which classifies the regions of the system's parameter space in which the observed behaviours occur, and found that the dynamics are well-organised. For the lowest flow rates investigated, the finger propagates steadily for all bubble sizes investigated. However, beyond a critical flow rate, a region of intermediately sized bubbles leads to lateral oscillations of the finger tip, thereby separating two regions of steadily propagating fingers. The smallest bubbles act as flow field perturbations in the vicinity of the finger's tip, leading to the selection of narrower fingers. The largest bubbles, in contrast, replace the finger's tip, leading to aggregate fingers with the same widths as would be selected without the bubble. The observations indicate that despite the presence of the bubble at its tip, the finger always adopts the equivalent-width, single-finger shape, as indicated by Couder *et al.* (1986). The region of oscillations, which occurs for an interval of intermediately sized bubbles, is bounded by the two regions of steadily propagating fingers. Depending on the flow rate and bubble size, the oscillations may be either periodic or disordered. For low flow rates, the finger's tip exhibits periodic oscillations centred about the channel's centreline, whilst

https://doi.org/10.1017/jfm.2025.10664 Published online by Cambridge University Press

secondary tip-splitting events can accompany the oscillations at higher flow rates. The loss of the steadily propagating state and onset of periodic oscillations, whose amplitude grows beyond onset, is dynamically consistent with a supercritical Hopf bifurcation.

We established the underlying physical mechanism that initially destabilises small bubbles, thereby leading to oscillations, by examining the curvature of the interface in the vicinity of the finger tip as the size of the bubble varies. We determined empirically that the steadily propagating finger destabilises when the curvature of the bubble's tip becomes smaller than that of the finger tip situated behind it, with this criterion occurring robustly for all investigated flow rates. When the curvatures are equal, there is no axial pressure drop along the bubble, and it becomes susceptible to lateral perturbations. The sideways movement of the finger couples with the deformability of the bubble, which provides a restoring mechanism to return the bubble back to the centreline of the channel, but the finger and bubble restoral mechanisms occur on different time scales, leading to the oscillations. The finger returns to steady propagation once the bubble has become sufficiently large such that it can effectively conform to the shape of the single-finger tip, thereby becoming part of the overall finger shape. At this point, the two restoral time scales are the same, and there is no longer a mechanism for oscillations.

The dynamics of individual bubbles in Hele-Shaw cells has recently been investigated by Wu *et al.* (2024) both experimentally and theoretically using a modified model of the liquid films around the bubble developed by Booth, Griffiths & Howell (2023). A key finding is that for the regime considered, the bubble speed is proportional to its radius. This result is relevant for the scaling of the critical flow rate of the second transition to oscillations with bubble size (see § 3.2), indicating that dynamics on the scale of the bubble is relevant at this transition point.

We have also presented preliminary evidence of the finger exhibiting disordered dynamics at the highest investigated flow rates. The finger's irregular motion in this regime appears to be orchestrated by unstable periodic states, as evidenced by the appearance of different short-lived periodic oscillations. Namely, we observed centred oscillations, which are identical to the stable periodic oscillations described at lower flow rates, and off-centred oscillations, in which the mean position of the finger's tip is biased towards one of the channel's side-walls. The disordered dynamics that we have observed is an interesting fluid mechanical phenomenon in its own right, and are consistent with our proposed hypothesis that unstable periodic states underpin the complex dynamics. However, because the periodic states are presumably unstable, this interpretation is purely speculative in the absence of a mathematical model and numerical simulations.

The original experiments by Couder *et al.* (1986) included preliminary observations of a different type of periodic oscillation, in which the bubble's shape pulsates as the finger propagates, leading to fingering patterns that are symmetric about $y = 0$; see figure 19. We only observed this mode of oscillation once in over two hundred experiments, occurring for a bubble whose size was close to the lower limit of what we were able to generate in our experiments; see the black star marker in figure 7. However, the original study indicated that the pulsation oscillations were frequently observed for small bubbles, and similar behaviour has also been observed in the radial geometry (Couder 1987). The elusiveness of this oscillation mode in our experiments is because the aspect ratio of our channel is smaller than that used by Couder *et al.* (1986), meaning that to achieve the same relative bubble sizes, smaller bubbles are required, and these are more difficult to access experimentally.

The phenomena that we have observed further highlight the inherent complexity contained in this conceptually simple system, whilst the propensity of this system to exhibit periodic dynamics renders it a suitable candidate for studying the transition to

https://doi.org/10.1017/jfm.2025.10664 Published online by Cambridge University Press

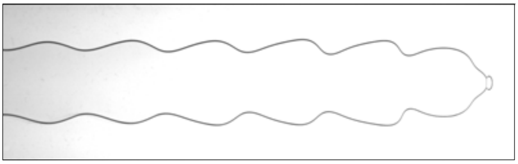

Figure 19. The periodically pulsating mode of propagation that was observed in one of our experiments. The bubble’s size is $r = 0.054$, and the dimensionless flow rate is $Q = \mu U_0^* / \sigma = 0.10$.

disordered dynamics. Future modelling attempts may be aided by the observation that the liquid films play a negligible role in the finger’s oscillations, because this suggests that two-dimensional models may be sufficient to capture the observed behaviours. However, the question remains as to whether similar mechanisms are responsible for a single Saffman–Taylor finger’s post-transition dynamics in the absence of a leading bubble.

Supplementary movies. Supplementary movies are available at https://doi.org/10.1017/jfm.2025.10664.

Funding. This work was supported via EPSRC grants EP/P026044/1 and EP/T008725/1, and an EPSRC DTP studentship (J.L.).

Declaration of interests. The authors report no conflict of interest.

REFERENCES

ARNÉODO, A., COUDER, Y., GRASSEAU, G., HAKIM, V. & RABAUD, M. 1989 Uncovering the analytical Saffman–Taylor finger in unstable viscous fingering and diffusion-limited aggregation. *Phys. Rev. Lett.* **63**, 984–987.

AUSSILLOUS, P. & QUÉRÉ, D. 2000 Quick deposition of a fluid on the wall of a tube. *Phys. Fluids* **12** (10), 2367–2371.

BEESON-JONES, T.H. & WOODS, A.W. 2019 Evidence for a universal saturation profile for radial viscous fingers. *Sci. Rep.* **9**, 7780.

BENSIMON, D. 1986 Stability of viscous fingering. *Phys. Rev. A* **33**, 1302–1308.

BISCHOFBERGER, I., RAMACHANDRAN, R. & NAGEL, S. 2014 Fingering versus stability in the limit of zero interfacial tension. *Nat. Commun.* **5**, 5265.

BOOTH, D.J., GRIFFITHS, I.M. & HOWELL, P.D. 2023 Circular bubbles in a Hele-Shaw channel: a Hele-Shaw Newton’s cradle. *J. Fluid Mech.* **954**, A21.

BOOTH, D.J., WU, K., GRIFFITHS, I.M., HOWELL, P.D., NUNES, J.K. & STONE, H.A. 2025 Bubble racing in a Hele-Shaw cell. *J. Fluid Mech.* **1010**, A19.

BRETHERTON, F.P. 1961 The motion of long bubbles in tubes. *J. Fluid Mech.* **10** (2), 166–188.

BUDANUR, N.B., SHORT, K.Y., FARAZMAND, M., WILLIS, A.P. & CVITANOVIĆ, P. 2017 Relative periodic orbits form the backbone of turbulent pipe flow. *J. Fluid Mech.* **833**, 274–301.

CHEN, J.-D. 1989 Growth of radial viscous fingers in a Hele-Shaw cell. *J. Fluid Mech.* **201**, 223–242.

CHEVALIER, C., AMAR, M.B., BONN, D. & LINDNER, A. 2006 Inertial effects on Saffman–Taylor viscous fingering. *J. Fluid Mech.* **552**, 83–97.

CHEVALIER, C., LINDNER, A. & CLÉMENT, E. 2007 Destabilization of a Saffman–Taylor fingerlike pattern in a granular suspension. *Phys. Rev. Lett.* **99**, 174501.

COMBESCOT, R. & DOMBRE, T. 1989 Selection in the anomalous Saffman–Taylor fingers induced by a bubble. *Phys. Rev. A* **39**, 3525–3535.

COUDER, Y. 1987 Anomalous Saffman–Taylor fingering. *Phys. Fluids* **30** (9), 2603–2603.

COUDER, Y. 2003 Viscous fingering as an archetype for growth patterns. In *Perspectives in Fluid Dynamics: A Collective Introduction to Current Research* (ed. G.K., Batchelor, H.K., Moffatt & M.G., Worster), pp. 53–98. Cambridge University Press.

COUDER, Y., GÉRARD, N. & RABAUD, M. 1986 Narrow fingers in the Saffman–Taylor instability. *Phys. Rev. A* **34** (6), 5175–5178.

CUTTLE, C., PIHLER-PUZOVIĆ, D. & JUEL, A. 2020 Dynamics of front propagation in a compliant channel. *J. Fluid Mech.* **886**, A20.

CVITANOVIĆ, P. & GIBSON, J.F. 2010 Geometry of the turbulence in wall-bounded shear flows: periodic orbits. *Phys. Scr.* **2010** (T142), 014007.

https://doi.org/10.1017/jfm.2025.10664 Published online by Cambridge University Press

DIAS, E.O., ALVAREZ-LACALLE, E., CARVALHO, M.S. & MIRANDA, J.A. 2012 Minimization of viscous fluid fingering: a variational scheme for optimal flow rates. *Phys. Rev. Lett.* **109**, 144502.

DUGUET, Y., PRINGLE, C.C.T. & KERSWELL, R.R. 2008 Relative periodic orbits in transitional pipe flow. *Phys. Fluids* **20** (11), 114102.

ECKHARDT, B., FAISST, H., SCHMIEGEL, A. & SCHNEIDER, T.M. 2008 Dynamical systems and the transition to turbulence in linearly stable shear flows. *Proc. R. Soc. Lond. A* **366** (1868), 1297–1315.

FONTANA, J.V., CUTTLE, C., PIHLER-PUZOVIĆ, D., HAZEL, A.L. & JUEL, A. 2024 Peeling fingers in an elastic Hele-Shaw channel. *J. Fluid Mech.* **985**, A1.

GAILLARD, A., KEELER, J.S., LE LAY, G., LEMOULT, G., THOMPSON, A.B., HAZEL, A.L. & JUEL, A. 2021 The life and fate of a bubble in a geometrically perturbed Hele-Shaw channel. *J. Fluid Mech.* **914**, A34.

GARDINER, B.P.J., MCCUE, S.W. & MORONEY, T.J. 2015 Discrete families of Saffman–Taylor fingers with exotic shapes. *Results Phys.* **5**, 103–104.

HAZEL, A.L., PAILHA, M., COX, S.J. & JUEL, A. 2013 Multiple states of finger propagation in partially occluded tubes. *Phys. Fluids* **25** (6), 062106.

HONG, D.C. & LANGER, J.S. 1987 Pattern selection and tip perturbations in the Saffman–Taylor problem. *Phys. Rev. A* **36**, 2325–2332.

JUEL, A., PIHLER-PUZOVIĆ, D. & HEIL, M. 2018 Instabilities in blistering. *Annu. Rev. Fluid Mech.* **50**, 691–714.

KAWAHARA, G., UHLMANN, M. & VAN VEEN, L. 2012 The significance of simple invariant solutions in turbulent flows. *Annu. Rev. Fluid Mech.* **44** (1), 203–225.

KEELER, J., THOMPSON, A., LEMOULT, G., HAZEL, A. & JUEL, A. 2019 The influence of invariant solutions on the transient behaviour of an air bubble in a Hele-Shaw channel. *Proc. R. Soc. Lond. A* **475** (2232), 20190434.

KOPF-SILL, A.R. & HOMSY, G.M. 1988 Nonlinear unstable viscous fingers in Hele-Shaw flows. I. Experiments. *Phys. Fluids* **31** (2), 242–249.

LAJEUNESSE, E. & COUDER, Y. 2000 On the tip-splitting instability of viscous fingers. *J. Fluid Mech.* **419**, 125–149.

LAWLESS, J., HAZEL, A.L. & JUEL, A. 2024 Periodic dynamics in viscous fingering. *Proc. R. Soc. Lond. A* **480**, 20240164.

LAWLESS, J., JUEL, A. & PIHLER-PUZOVIĆ', D. 2025 Nonlinear dynamics of viscous fingering. *Physica D* **476**, 134631.

LAWLESS, J., KEELER, J.S., GAILLARD, A., HAZEL, A.L. & JUEL, A. 2022 The unpredictable nature of bubble evolution. *Sci. Rep.* **12**, 20752.

MATHIESEN, J., PROCACCIA, I., SWINNEY, H.L. & THRASHER, M. 2006 The universality class of diffusion-limited aggregation and viscous fingering. *Eur. Phys. Lett.* **76**, 257–263.

MCCLOUD, K.V. & MAHER, J.V. 1995 Pattern selection in an anisotropic Hele-Shaw cell. *Phys. Rev. E* **51**, 1184–1190.

MONNET, B., MADEC, C., VIDAL, V., JOUBAUD, S. & JEROME, J. 2022 Bubble rise in a Hele-Shaw cell: bridging the gap between viscous and inertial regimes. *J. Fluid Mech.* **942**, R3.

PAILHA, M., HAZEL, A.L., GLENDINNING, P. & JUEL, A. 2012 Oscillatory bubbles induced by geometrical constraint. *Phys. Fluids* **24** (2), 021702.

PARK, C.W. & HOMSY, G.M. 1985 The instability of long fingers in Hele-Shaw flows. *Phys. Fluids* **28** (6), 1583–1585.

PATERSON, L. 1981 Radial fingering in a Hele-Shaw cell. *J. Fluid Mech.* **113**, 513–529.

PITTS, E. 1980 Penetration of fluid into a Hele-Shaw cell: the Saffman–Taylor experiment. *J. Fluid Mech.* **97** (1), 53–64.

RABAUD, M., COUDER, Y. & GERARD, N. 1988 Dynamics and stability of anomalous Saffman–Taylor fingers. *Phys. Rev. A* **37**, 935–947.

ROMERO, L. 1982 The fingering problem in a Hele-Shaw cell. *PhD thesis*, California Institute of Technology, California, USA.

SAFFMAN, P.G. & TAYLOR, G.I. 1958 The penetration of a fluid into a porous medium or Hele-Shaw cell containing a more viscous liquid. *Proc. R. Soc. Lond. A* **245**, 312–329.

SURI, B., KAGEORGE, L., GRIGORIEV, R.O. & SCHATZ, M.F. 2020 Capturing turbulent dynamics and statistics in experiments with unstable periodic orbits. *Phys. Rev. Lett.* **125**, 064501.

TABELING, P., ZOCCHI, G. & LIBCHABER, A. 1987 An experimental study of the Saffman–Taylor instability. *J. Fluid Mech.* **177**, 67–82.

THOMÉ, H., COMBESCOT, R. & COUDER, Y. 1990 Controlling singularities in the complex plane: experiments in real space. *Phys. Rev. A* **41**, 5739–5742.

https://doi.org/10.1017/jfm.2025.10664 Published online by Cambridge University Press

Vanden-Broeck, J.-M. 1983 Fingers in a Hele-Shaw cell with surface tension. *Phys. Fluids* **26** (8), 2033–2034.

Vasconcelos, G.L. 1999 Motion of a finger with bubbles in a Hele-Shaw cell: an exact solution. *Phys. Fluids* **11** (6), 1281–1283.

Vasconcelos, G.L. 2000 Analytic solution for two bubbles in a Hele-Shaw cell. *Phys. Rev. E* **62**, R3047–R3050.

Vasconcelos, G.L. 2015 Multiple bubbles and fingers in a Hele-Shaw channel: complete set of steady solutions. *J. Fluid Mech.* **780**, 299–326.

Wu, K., Booth, D.J., Griffiths, I.M., Howell, P.D., Nunes, J.K. & Stone, H.A. 2024 Motion and deformation of a bubble in a Hele-Shaw cell. *Phys. Rev. Fluids* **9**, 123603.

Zhang, J.H. & Liu, Z.H. 1998 Study of the relationship between fractal dimension and viscosity ratio for viscous fingering with a modified DLA model. *J. Petrol. Sci. Engng* **21** (1), 123–128.

Zheng, Z., Kim, H. & Stone, H.A. 2015 Controlling viscous fingering using time-dependent strategies. *Phys. Rev. Lett.* **115**, 174501.

Zocchi, G., Shaw, B.E., Libchaber, A. & Kadanoff, L.P. 1987 Finger narrowing under local perturbations in the Saffman–Taylor problem. *Phys. Rev. A* **36**, 1894–1900.

https://doi.org/10.1017/jfm.2025.10664 Published online by Cambridge University Press